A Broadband and Scalable Lumped Element Model for Fully Symmetric Inductors Under Single-Ended and Differentially Driven Operations

Jyh-Chyurn Guo and Teng-Yang Tan

***Abstract*—A broadband and scalable 2-T model is developed to accurately simulate fully symmetric inductors with various dimensions. The 2-T model is defined to reflect the structure of an equivalent circuit with two identical T-model circuits. Two-step de-embedding is assisted by open and through pads for extraction of intrinsic characteristics. The accuracy is validated by 3-D full-wave electromagnetic simulation. A novel parameter extraction flow is established, and a single set of model parameters is derived to be valid for both single-ended and differentially driven topologies. The broadband accuracy is proven by a good match with S-parameters, $L(\omega)$, $Re(Z_{\rm in}(\omega))$, and $Q(\omega)$ over frequencies up to 20 GHz. The scalability is justified by good fitting with either a linear or a parabolic function of spiral coil radii. Furthermore, all model parameters are frequency independent so as to ensure computation efficiency. This 2-T model consistently predicts the enhancement of $Q_{\rm max}$ by 20%–30% for the symmetric inductors under a differential excitation. The Q improvement is even better than 100% over broader frequencies beyond $f_m(Q_{\rm max})$.**

***Index Terms*—Broadband, differential, inductor, scalable, single end, symmetric.**

I. Introduction

ON-CHIP symmetric inductors become increasingly important for a low-noise and low-power RF circuit design [1]–[4]. The symmetric passive elements such as inductors and varactors that operate under a differential excitation can achieve better noise immunity and meet stringent requirements of matching and common mode rejection. Given the voltage-controlled oscillator design as an example, the adoption of differential inductors can realize advantages such as lower phase noise due to a higher Q, larger tuning range attributed to a higher self-resonance frequency $(f_{\rm SR})$, and saving of single-end to differential conversion circuitry for the local oscillator drive of a Gilbert-cell mixer [1], [5]. For conventional differential inductors, a number of crossover and cross-under connections are used to join groups of coupled metal traces from one side of an axis of symmetry to the other [6]–[10]. Unfortunately, this connection method generally causes mismatch between port 1 and port 2 [11] due to the fact that the conventional differential inductors are actually not truly symmetric in geometry, as well as structure, and a fully symmetric inductor with new layout was proposed to improve the symmetry in terms of two-port S-parameters [11]. However, the degraded Q, compared with the conventional ones, appears as a weakness to be solved. The requirement of an accurate and computation-efficient model to fit both single-end and differential operations emerges as another challenge to the on-Si-chip symmetric inductors for RF circuit simulation and design. A lumped element equivalent circuit model was proposed to simulate the symmetric inductors with SPICE-compatible efficiency [12]. However, different model parameters that are required for single-end and differential topologies manifest themselves unphysical and incur difficulty in prediction. Furthermore, the scalability to fit various geometries was not verified and demonstrated.

In this paper, a 2-T model has been developed as a successful extension of our original T-model for spiral inductors [13]. This 2-T model is composed of a pair of identical spiral coil resistance–inductance–capacitance (RLC) networks and a substrate RLC network shared by the pair of spiral coils. It can realize the features of broadband accuracy and scalability. A novel parameter extraction flow was established through equivalent circuit analysis under differential and single-end excitations. The differential excitation can drive the on-chip inductor free from substrate loss and can facilitate parameter extraction due to the elimination of substrate network. A single set of model parameters can fit both single-ended and differentially driven topologies. The broadband accuracy is extensively verified by S-parameters, $L(\omega)$, $Re(Z_{\rm in}(\omega))$, and $Q(\omega)$ over frequencies up to 20 GHz for all varying dimensions. The scalability is justified by good fitting with either a linear or a parabolic function of spiral coil radii. Furthermore, all model parameters are frequency independent to enable easy deployment in the circuit simulator. This 2-T model consistently predicts the improvement of the maximum quality factor $(Q_{\rm max})$ by 20%–30% for the symmetric inductors under the differential excitation. The Q improvement is even better than 100% over a broader bandwidth beyond $f_m(Q_{\rm max})$. This scalable model can facilitate an optimal design of symmetric inductors through model parameters that are relevant to various geometries. Furthermore, the broadband accuracy that is proven by both single-end and differential excitations is useful for widely used differential topologies

Manuscript received February 6, 2007; revised April 3, 2007. This work was supported in part by the National Science Council under Grant 95-2221-E009-289. The review of this paper was arranged by Editor M. J. Kumar.

The authors are with the Department of Electronics Engineering, National Chiao-Tung University, Hsinchu 30010, Taiwan, R.O.C. (e-mail: jcguo@mail.nctu.edu.tw).

Color versions of one or more of the figures in this paper are available online at http://ieeexplore.ieee.org.

Digital Object Identifier 10.1109/TED.2007.900005

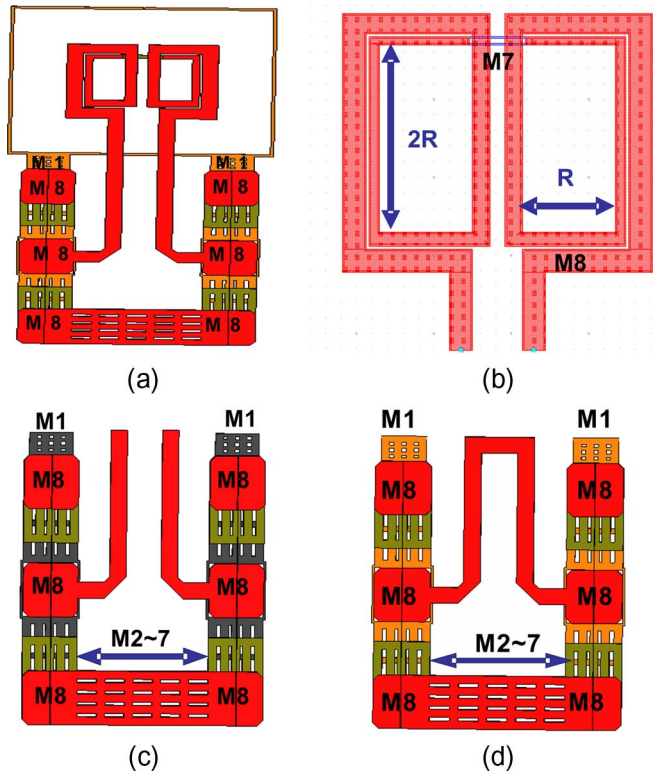

Fig. 1. Layout of a fully symmetric inductor and dummy pads for de-embedding. (a) Full structure of the intrinsic inductor and pads. (b) Intrinsic inductor of the taper structure with varying metal trace widths ($5-15$ μm). (c) Open pads. (d) Through pads.

and can improve the RF circuit simulation accuracy that is demanded by a broadband design.

II. New Symmetric Inductor Structure Design and Fabrication Technology

A new fully symmetric inductor with a taper structure was fabricated by the 0.13-μm back-end-of-line (BEOL) technology with eight layers of Cu and fluorinated silicate glass intermetal dielectric (IMD) with $k = 3.8$. The top metal of a 3-μm Cu was used to implement the spiral coils for minimizing the series resistance. The layout of the symmetric inductor, open and through pads for de-embedding, and the full structure that consists of intrinsic device and pads are illustrated in Fig. 1. For the new fully symmetric inductor shown in Fig. 1(b), a taper structure with varying metal trace widths is the primary enhancement over the original one [11] to solve the weakness of degraded Q.

Electromagnetic (EM) simulation was done to identify the mechanism that underlies Q degradation. To ensure the accuracy of EM simulation, calibration was performed with appropriate modification on the model parameters. Table I summarizes the model parameters that are used in EM simulation and the default process parameters in the technology file for the 0.13-μm BEOL process. The comparison indicates a minor adjustment on the metal resistivities for metal 8 (M8) and metal 7 (M7), as well as IMD thickness for levels 1–6. The major calibration happened to the IMD7 thickness. The shift from the default process parameter is around 10%. Considering

TABLE I
Model Parameters Used in the EM Simulation and the Comparison With the Default Process Parameters in the Technology File for the 0.13-μm BEOL Process. The Parameters Include the Resistivities and Thicknesses for the Si Substrate, M7, and M8, as well as Dielectric Constants and Thicknesses for the IMD [Levels 1–6 (IMD1–6) and Level 7 (IMD7)]

Materials	Parameters	Technology file process parameters	EM simulation model parameters
Si substrate	ρ_{Si}(Ω-cm)	10	10
	t_{Si} (μm)	600	600
M8	ρ_{M8}(Ω-cm)	1.719×10^{-6}	1.61×10^{-6}
	t_{M8} (μm)	3	3
M7	ρ_{M7}(Ω-cm)	1.8×10^{-6}	1.71×10^{-6}
	t_{M7} (μm)	0.9	0.9
IMD1~6	$t_{IMD1\sim6}$ (μm)	1.5	1.4
	$K_{IMD1\sim6}$	3.8	3.8
IMD7	t_{IMD7} (μm)	6.02	6.8
	K_{IMD7}	3.8	3.8

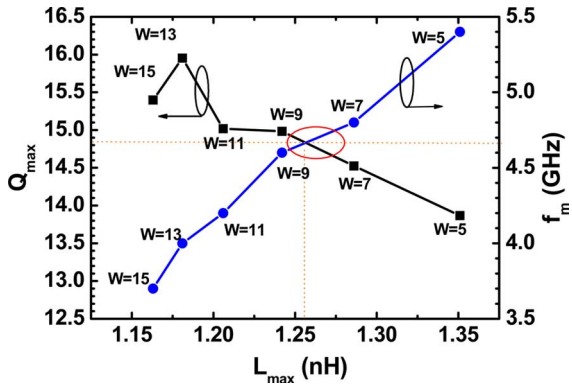

Fig. 2. $Q_{\max}$ and f_m versus $L_{\max}$ calculated by EM simulation (advanced design system momentum) for the taper inductor optimization design.

the frequency-dependent skin depth, dynamic regridding and "solve inside" were carried out in the EM simulation to ensure a sufficient mesh density. For the 3-μm Cu as the metal coils, the skin depth decreases from nearly 2 μm at 1 GHz to 0.45 μm at 20 GHz. The mesh density achieved under dynamic regridding is ensured with grid size smaller than the skin depth under varying frequencies.

The EM simulation that is based on the mentioned calibration reveals that the opposite current flows in two inner adjacent metal traces with much shorter distance in the proposed new layout [11] lead to degraded magnetic flux. This result explains Q degradation suffered by the fully symmetric inductors compared with the conventional ones [6]–[10]. Again, EM simulation was performed to guide the layout modification and optimization for Q improvement. The idea to overcome the weakness is to use wider metal traces in the nearest side and narrower ones in the far side. The wider metal can mitigate the proximity-effect-induced resistive loss and Q degradation. On the other hand, the narrower metal can compensate for the frequency ($f_{\rm SR}$ and f_m) degradation. Herein, $f_{\rm SR}$ and f_m are the frequencies that correspond to self-resonance and $Q_{\max}$, respectively. Fig. 2 demonstrates the EM simulation results for uniform symmetric inductors with identical widths for

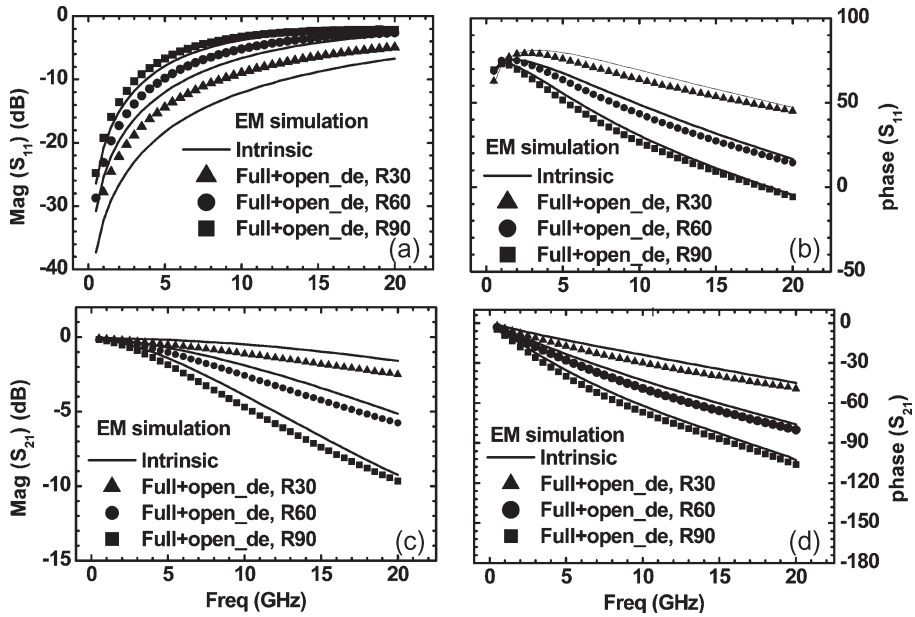

Fig. 3. Comparison between the full structure after open de-embedding and the intrinsic inductor. (a) Mag(S_{11}). (b) Phase(S_{11}). (c) Mag(S_{21}). (d) Phase(S_{21}).

every metal trace. Apparently, the varying metal trace widths lead to a tradeoff between $Q_{\max}$ and f_m. The wider width contributes a higher $Q_{\max}$ but simultaneously suffers a lower f_m. The simulation reveals a compromised point between 7 and 9 μm, i.e., around 8 μm, and suggests that optimization can be done through a taper structure. The optimization target for an inductor design is to enhance Q and maintain $f_{\rm SR}$ to be sufficiently high. The taper structure with gradual variation of metal trace widths is proposed to simultaneously increase the inductance, reduce the coupling capacitance, and minimize the series resistance.

According to the guideline, taper structures, as shown in Fig. 1(b), are designed with a total of seven metal traces in which the trace width varies from 5 to 15 μm by a step of 2 μm between every two adjacent traces. The intertrace space is fixed at 2 μm, and inner radii with $R = 30,\ 60,$ and 90 μm are layout split for $Q_{\max}$ and $f_{\rm SR}$ tuning as well as scalability verification. The physical inductances achieved at a sufficiently low frequency are around 0.6–1.9 nH, which corresponds to $R = 30{-}90$ μm. Two parallel metal traces existing in the full structure [Fig. 1(a)], which started from the signal pads and ended at the boundary of intrinsic inductors, suggest that through de-embedding is indispensable and particularly critical for small inductors.

Note that a guard ring (GR) that is fabricated by metal 1 (M1) was employed in the full structure [Fig. 1(a)] to serve as a ground cage for the intrinsic device. This GR was removed, together with the intrinsic device from both open and through pads [Fig. 1(c) and (d)]. It was assumed that this GR effect on open and through pads is insignificant. EM simulation was carried out to verify the assumption, and the results indicate very minor differences in the S-parameters for open and through pads between those with and without GR ($< 2\%$ for open pads and nearly identical for through pads). As a result, the EM simulation validates the assumption and the following de-embedding method.

III. Characterization and Two-Step De-Embedding

S-parameters were measured by using an Agilent network analyzer up to 20 GHz for the full structure and dummy pads with and without intrinsic inductors, respectively. A good symmetry is justified by the measured two-port S-parameters with a mismatch between S_{11} and S_{22} (magnitude and phase) $<$ 2% for $R = 30$ μm and $< 1\%$ for $R = 60$ and 90 μm. An even better symmetry is demonstrated for S_{12} and S_{21} (magnitude and phase) with a mismatch $< 0.5/0.4/0.3\%$ that corresponds to $R = 30/60/90$ μm over a full range of frequency to 20 GHz.

Two-step de-embedding was assisted by open and through pads in Fig. 1(c) and (d) to extract the truly intrinsic characteristics for parameter extraction and modeling. Three-dimensional full-wave EM simulation was performed using the Ansoft high-frequency structure simulator (HFSS) to investigate the influence of open and through de-embedding on the high-frequency characteristics of the fully symmetric inductors. First, the de-embedding effect was verified by two-port S-parameters. Fig. 3 shows S_{11} and S_{21} (magnitude and phase) that are simulated for a full structure subject to open de-embedding and the comparison with intrinsic characteristics. The substantial deviation suggests that open de-embedding only cannot extract the truly intrinsic feature. Then, two-step de-embedding that simultaneously incorporates open and through de-embedding was carried out. The excellent match demonstrated in Fig. 4 for S_{11} and S_{21} validates the two-step de-embedding.

In addition to the S-parameters, three more key parameters such as $L(\omega)$, $Re(Z_{\rm in}(\omega))$, and $Q(\omega)$ were verified for rigorous certification. Fig. 5 presents the simulation results in terms of $L(\omega)$ and $Re(Z_{\rm in}(\omega))$. Consistently, open de-embedding only

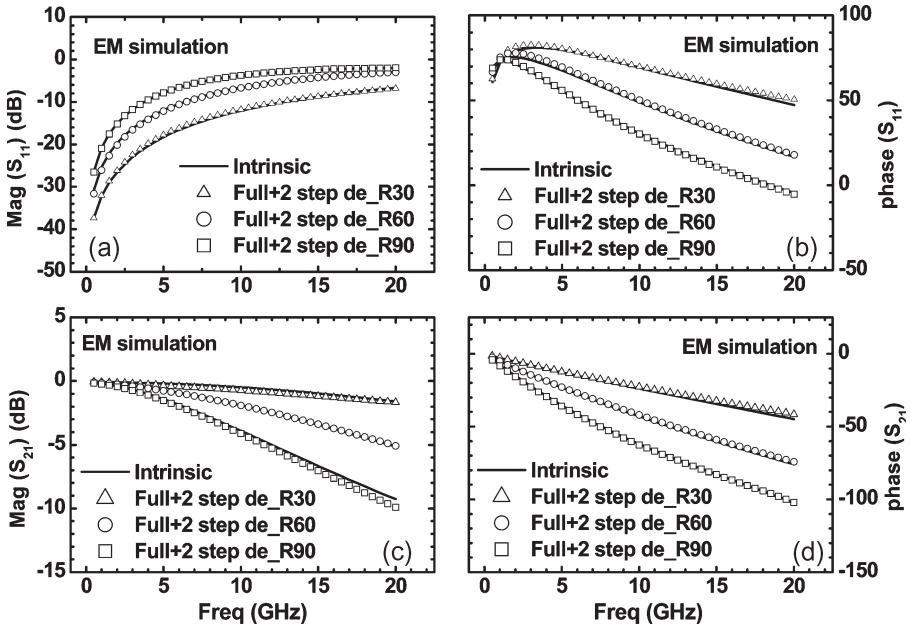

Fig. 4. Comparison between the full structure after two-step de-embedding and the intrinsic inductor. (a) Mag(S_{11}). (b) Phase(S_{11}). (c) Mag(S_{21}). (d) Phase(S_{21}).

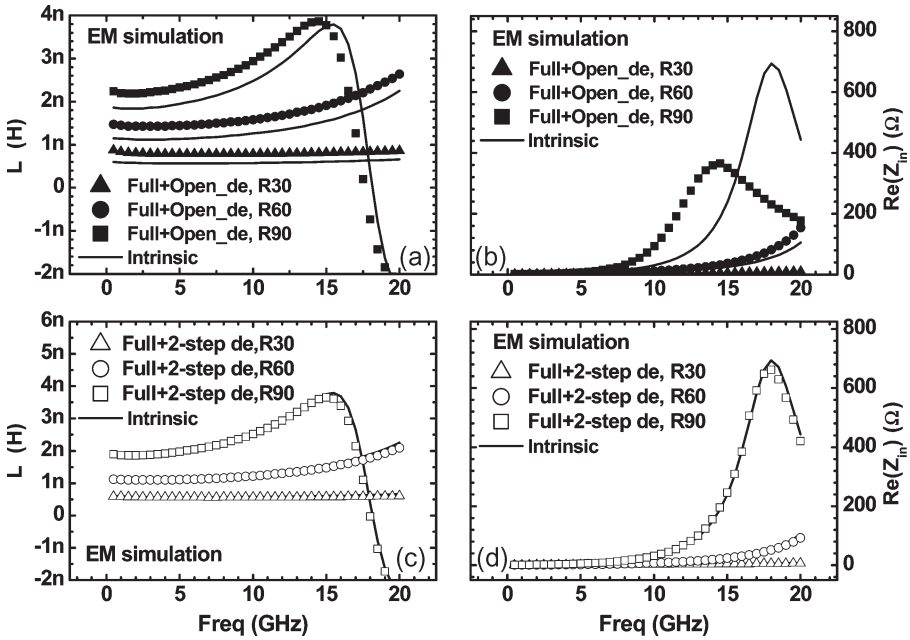

Fig. 5. Comparison between the full structure after open de-embedding and the intrinsic inductor for (a) $L(\omega)$ and (b) $Re(Z_{\rm in}(\omega))$ and between the full structure after two-step de-embedding and the intrinsic inductor for (c) $L(\omega)$ and (d) $Re(Z_{\rm in}(\omega))$. EM simulation is done by HFSS for inductors with various R's (i.e., 30, 60, and 90 μm).

reveals dramatic deviation from the intrinsic characteristics shown in Fig. 5(a) and (b), whereas the two-step de-embedding that involves both open and through pads can fix the deviation and yield an excellent match with the original intrinsic features shown in Fig. 5(c) and (d) for the symmetric inductors with various R (i.e., 30, 60, and 90 μm). More extensive verification was done in terms of $Q(\omega)$. Again, the error suffered by open de-embedding only in Fig. 6(a) can be effectively suppressed and recovered to a good match shown in Fig. 6(b) by adopting the two-step de-embedding. As a result, 3-D EM simulation justifies that the two-step de-embedding assisted by carefully designed open and through pads can precisely extract the truly intrinsic characteristics.

IV. 2-T Model's Equivalent Circuit and Model Parameter Extraction Flow

Fig. 7(a) illustrates the equivalent circuit schematics of the 2-T model proposed for on-chip fully symmetric inductors. A pair of identical RLC networks represents the symmetric spiral coils, and a substrate RLC network is commonly shared by the pair of spiral coils. The capacitances $C_{\rm ox,1,2,3}$ deployed

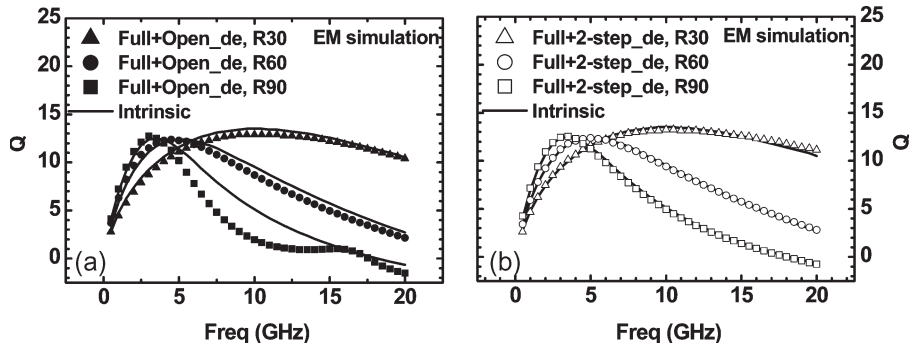

Fig. 6. Comparison of simulated $Q(\omega)$ (a) between the full structure after open de-embedding and the intrinsic inductor and (b) between the full structure after two-step de-embedding and the intrinsic inductor. EM simulation is done by HFSS for inductors with various R's (i.e., 30, 60, and 90 μm).

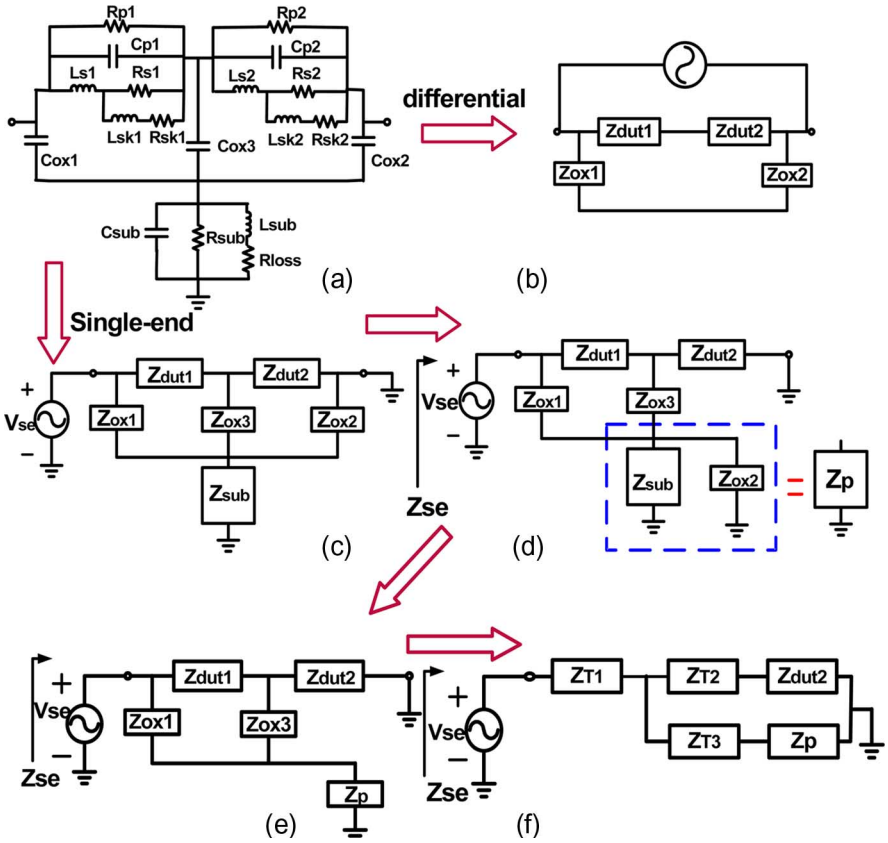

Fig. 7. 2-T model. (a) Original equivalent circuit schematics. (b) Reduced circuit block under differential excitation. (c) Circuit block under single-end excitation. (d) Transformation from (c) for model parameter extraction. (e) Equivalent circuit topology of (d). (f) Topology conversion from the π-circuit of $Z_{\rm dut1}$, $Z_{\rm ox1}$, and $Z_{\rm ox3}$ to the T-circuit of $Z_{\rm T1}$, $Z_{\rm T2}$, and $Z_{\rm T3}$.

between the pair of spiral coil networks and substrate network account for the coupling between the spiral inductors and lossy substrate underneath. The 2-T model is an extension of our original T-model for single-end spiral inductors [13]. The major enhancement is the adoption of one pair of series $R_{\rm sk}$ and $L_{\rm sk}$ to simulate the metal coil proximity-induced eddy current effect, which is originated from augmented EM coupling between two closely placed spiral coils. As a result, the physical elements that compose the spiral coil network increase to six (i.e., R_S, L_S, R_p, C_p, $R_{\rm sk}$, and $L_{\rm sk}$), whereas those of the substrate network are kept at four (i.e., $C_{\rm sub}$, $R_{\rm sub}$, $R_{\rm loss}$, and $L_{\rm sub}$).

The original circuit schematics can be mapped to the topologies consisting of $Z_{\rm dut1,2}$, $Z_{\rm ox1,2,3}$, and $Z_{\rm sub}$ shown in Fig. 7(b) and (c), which correspond to differential and single-end excitations, respectively. $Z_{\rm dut1}$ and $Z_{\rm dut2}$ represent the RLC networks for the pair of symmetric spiral coils, and $Z_{\rm sub}$ accounts for the lossy substrate. $Z_{\rm ox1} = Z_{\rm ox2} = Z_{\rm ox3} = 1/j\omega C_{\rm ox}$ act as the coupling path between $Z_{\rm dut1,2}$ and $Z_{\rm sub}$. This 2-T model, which is as an easy extension of the original T-model for single-end spiral inductors, is targeted to fit the fully symmetric inductor under either a single-ended or a differentially driven operation. For the differential excitation, with the signals being 180° out of phase applied at two ports, $Z_{\rm sub}$ and $Z_{\rm ox3}$ can be neglected, and then the differential input impedance Z_d is simplified to a parallel combination of $(Z_{\rm dut1} + Z_{\rm dut2})$ and $(Z_{\rm ox1} + Z_{\rm ox2})$, as shown in Fig. 7(b). This simplified circuit

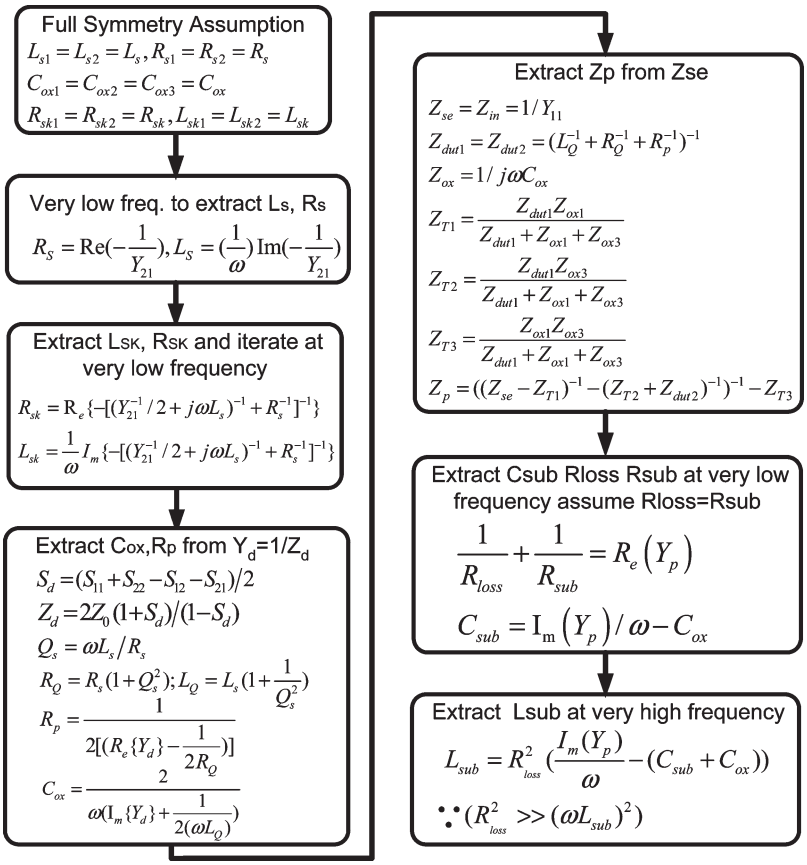

Fig. 8. 2-T model parameter formulas and extraction flow chart.

topology helps reduce the extraction flow and enable extraction of spiral coil network elements. As for the single-end excitation, the existence of $Z_{\rm sub}$ and $Z_{\rm ox3}$ in Fig. 7(c) makes the circuit analysis more sophisticated, which is indispensable for the extraction of the substrate network elements. Circuit transformation from Fig. 7(c) and (d) and followed by π-to-T topology conversion illustrated by Fig. 7(e) and (f) will be performed to enable the substrate network parameter extraction.

Based on the circuit topology conversion and analysis, the model parameters can be extracted through the flow in Fig. 8, which includes equations to derive each model parameter. Attributed to the symmetric nature, all the elements that appear at both sides are assumed identical to simplify the problem. In the first phase, a simplified circuit topology that is valid under a differential excitation, i.e., Fig. 7(b), was adopted to extract six elements in $Z_{\rm dut1,2}$ and $C_{\rm ox}$ in $Z_{\rm ox1,2}$. First, R_S and L_S can be extracted from $Re(-1/Y_{21})$ and $Im(-1/Y_{21})$ under a very low frequency, where $C_{\rm ox}$ is negligible. Afterward, proximity effect elements $R_{\rm sk}$ and $L_{\rm sk}$ are introduced in the equations of Y_{21} and initially extracted R_S and L_S for re-extraction, as well as necessary update to R_S and L_S through iteration. Finally, R_p and $C_{\rm ox}$ can be extracted from the equations of $Y_d(=1/Z_d)$, R_Q, and L_Q (function of R_S and L_S). In the second phase, the full circuit topology that is appropriate for a single-end excitation by incorporating both spiral coil and substrate networks in Fig. 7(c) was employed to extract the remaining circuit elements for $Z_{\rm sub}$. Following an easy transformation from Fig. 7(c) and (d) that is succeeded by π-to-T topology conversion illustrated in Fig. 7(e) and (f), Z_{T1}, Z_{T2}, and Z_{T3} can be derived from $Z_{\rm dut1}$, $Z_{\rm ox1}$, and $Z_{\rm ox3}$. Subsequently, $Z_p = Z_{\rm sub}//Z_{\rm ox2}$ can be extracted from the measured $Z_{\rm se}=1/Y_{11}$, as well as the known $Z_{\rm dut1,2}$ and $Z_{\rm ox1,3}$. Note that $Z_{\rm se}$ is the input impedance that corresponds to the single-end topology. To the end, three of the substrate network elements $C_{\rm sub}$, $R_{\rm sub}$, and $R_{\rm loss}$ can be extracted from the equations of $Re(1/Z_p)$ and $C_{\rm ox}$ under a very low frequency, provided that $\omega L_{\rm sub}$ was negligible. Then, $L_{\rm sub}$ can be extracted from the equation of $Im(1/Z_p)$ and the known $C_{\rm sub}$, $R_{\rm loss}$, and $C_{\rm ox}$.

All the model parameters that were extracted through the first run of flow just serve as the initial guess for further optimization through best fitting to the measured S-parameters, $L(\omega)$, $Re(Z_{\rm in}(\omega))$, and $Q(\omega)$.

V. Broadband Accuracy, Differential Mode Q Improvement, and Scalability

The broadband accuracy and the scalability of model parameters have been extensively verified and will be presented in this section. Furthermore, the improvement of Q and $f_{\rm SR}$ that is realized by a differential topology compared with the single-end counterpart will be analyzed through our 2-T model equivalent circuit analysis.

A. 2-T Model Broadband Accuracy

The 2-T model that was developed for fully symmetric inductors has been verified by comparison with measurement

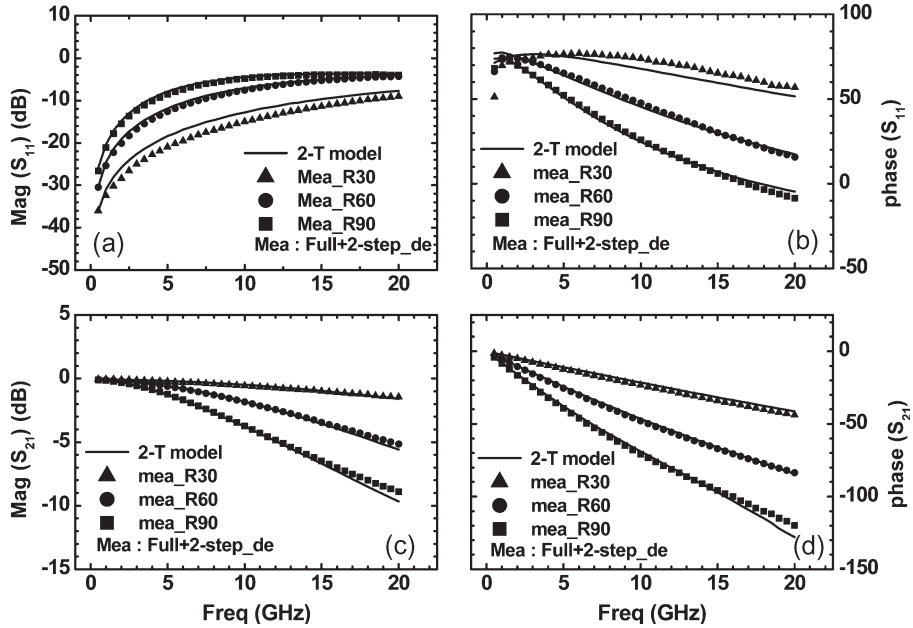

Fig. 9. Comparison between the 2-T model and the measurement for S_{11} and S_{21} of fully symmetric inductors with various R's (i.e., 30, 60, and 90 μm). (a) Mag(S_{11}). (b) Phase(S_{11}). (c) Mag(S_{21}). (d) Phase(S_{21}).

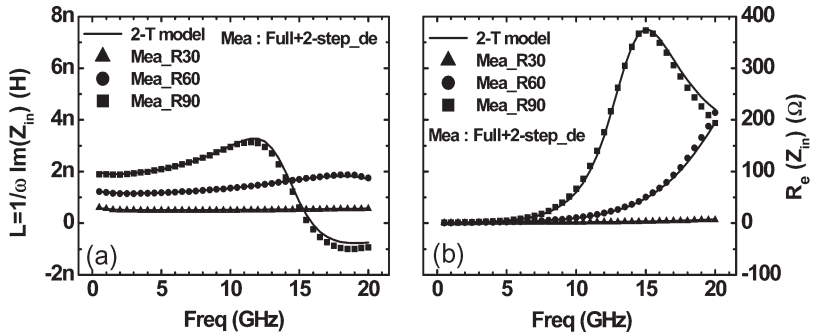

Fig. 10. Comparison between the 2-T model and the measurement for fully symmetric inductors under a single-end excitation. (a) $L(\omega) = Im(Z_{\rm in}(\omega))$. (b) $Re(Z_{\rm in}(\omega))$.

in terms of S-parameters, $Re(Z_{\rm in}(\omega))$, $L(\omega)$, and $Q(\omega)$ for both single-end and differential excitations over wideband up to 20 GHz. Fig. 9(a)–(d) indicates the comparison for S_{11} and S_{21} between the 2-T model and the measurement subject to two-step de-embedding. A good match is achieved for all coil radii. It is even better matched as compared with EM simulation before dedicated calibration. More extensive verification has been done by comparison of three key parameters for spiral inductors, i.e., $L(\omega)(= Im(Z_{\rm in}(\omega)/\omega)$, $Re(Z_{\rm in}(\omega))$, and $Q(\omega)]$. The quality factor $Q(\omega)$ is defined by $\omega L(\omega)/Re(Z_{\rm in}(\omega))$. All three parameters are frequency dependent, which is critically related to the spiral conductor loss and Si substrate loss. Fig. 10 illustrates the excellent fit to the measured $L(\omega)$ and $Re(Z_{\rm in}(\omega))$ under the single-end excitation for all inductors operating up to 20 GHz. The transition from inductive to capacitive mode at $f > f_{\rm SR}$ is accurately reproduced for the largest inductor ($f_{\rm SR} = 16$ GHz for $R = 90$ μm). Moreover, the model can exactly capture the full band behavior of $Re(Z_{\rm in}(\omega))$ even beyond self-resonance, such as the dramatic increase prior to resonance, peak at resonance, and then sharp drop beyond the peak.

Regarding the differential excitation, the 2-T model accuracy is again certified by a good match with the measurement in terms of $Re(S_d)$, $Im(S_d)$, $L_d = Im(Z_d)/\omega$, and $Re(Z_d)$ shown in Fig. 11(a)–(d). The equations to derive S_d and Z_d from two-port S-parameters can be referred to the extraction flow in Fig. 8. Both $Re(S_d)$ and $Im(S_d)$ reveal significant dependence on the coil radii. The smallest inductor with $R = 30$ μm indicates good linearity with respect to frequency, whereas the larger ones ($R = 60$ and 90 μm) exhibit a nonlinear feature with an obvious peak followed by a falloff that accounts for the occurrence of self-resonance. Furthermore, Fig. 12 presents a promisingly good prediction to the impedance of the pair of symmetric spiral coils, i.e., $Z_{\rm dut1}$ and $Z_{\rm dut2}$, for *different dimensions* of inductors ($R = 30$, 60, and 90 μm). The results justify that the proposed 2-T model can capture the broadband behavior subject to both single-end and differential excitations over frequencies up to 20 GHz. Again, all the measured parameters are intrinsic ones that are extracted through the proven two-step de-embedding.

Note that the larger deviation that appears in $Im(Z_d)$ for the largest inductor ($R = 90$ μm) in very high frequencies beyond

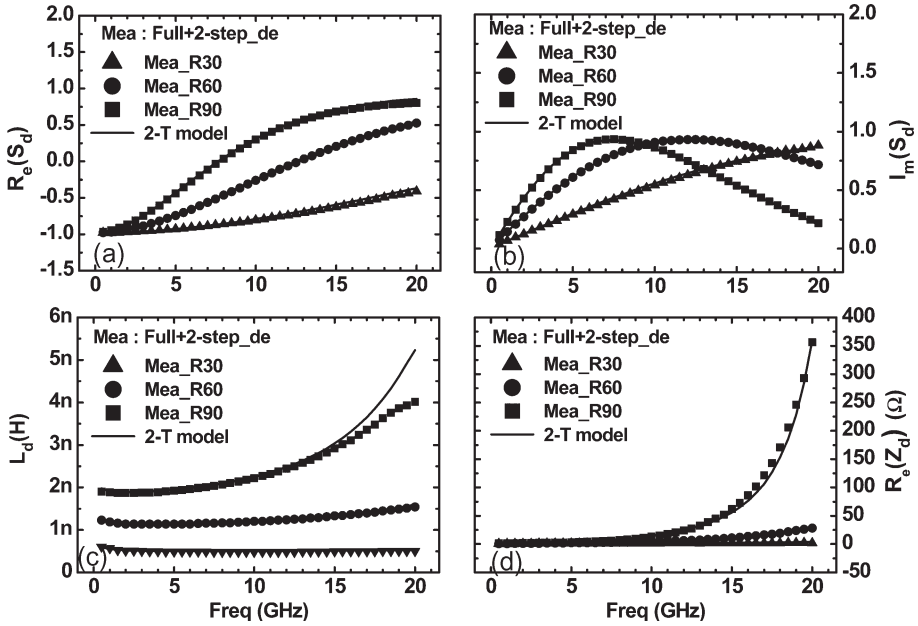

Fig. 11. Comparison between the 2-T model and the measurement for fully symmetric inductors under differential excitation. (a) $Re(S_d)$. (b) $Im(S_d)$. (c) $L_d = Im(Z_d)/\omega$. (d) $Re(Z_d)$.

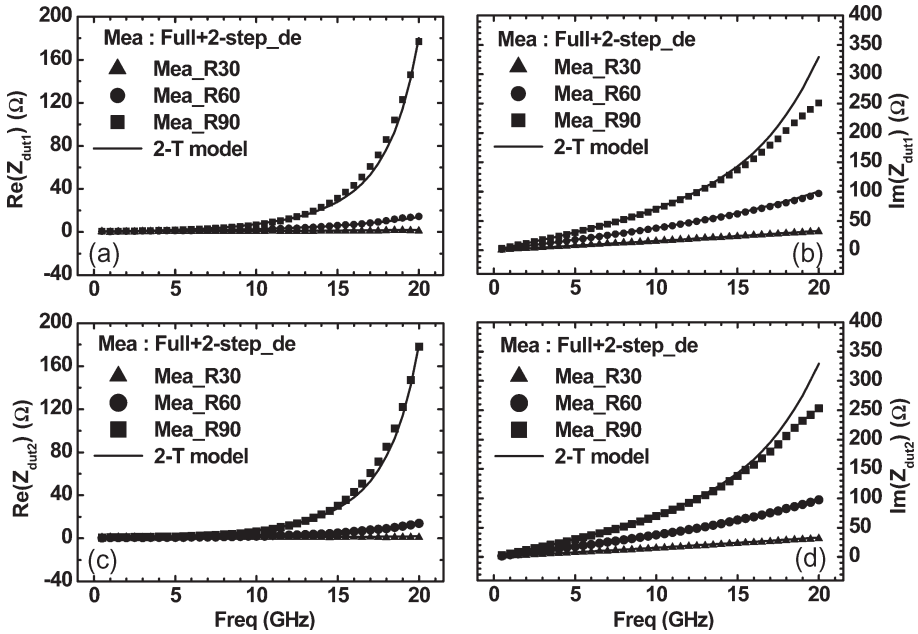

Fig. 12. Comparison between the 2-T model and the measurement for fully symmetric inductors under differential excitation. (a) $Re(Z_{\mathrm{dut1}})$. (b) $Im(Z_{\mathrm{dut1}})$. (c) $Re(Z_{\mathrm{dut2}})$. (d) $Im(Z_{\mathrm{dut2}})$.

15 GHz [Fig. 12(c)] was generated through the calculation from S_d to Z_d following the equation $Z_d = 2Z_0(1+S_d)/(1-S_d)$ in Fig. 8. For S_d as one of the target parameters for fitting, a good match is achieved in both $Re(S_d)$ and $Im(S_d)$ with an error below 6 for all inductors ($R = 30,\ 60,$ and 90 μm) over a full range of frequency to 20 GHz. However, for Z_d derived from S_d, the computation of $(1+S_d)/(1-S_d)$ may amplify the error due to the opposite sign of error in the denominator and numerator. Model parameter tuning with an increasing weighting factor on fitting Z_d can solve this weakness.

B. Differential Mode Q Improvement

Eventually, $Q(\omega)$ is the most critical parameter governing RF integrated circuit performance such as power, gain, and noise figure. Fig. 13(a) and (b) demonstrates a promisingly good match with the measured $Q(\omega)$ for both single-end and

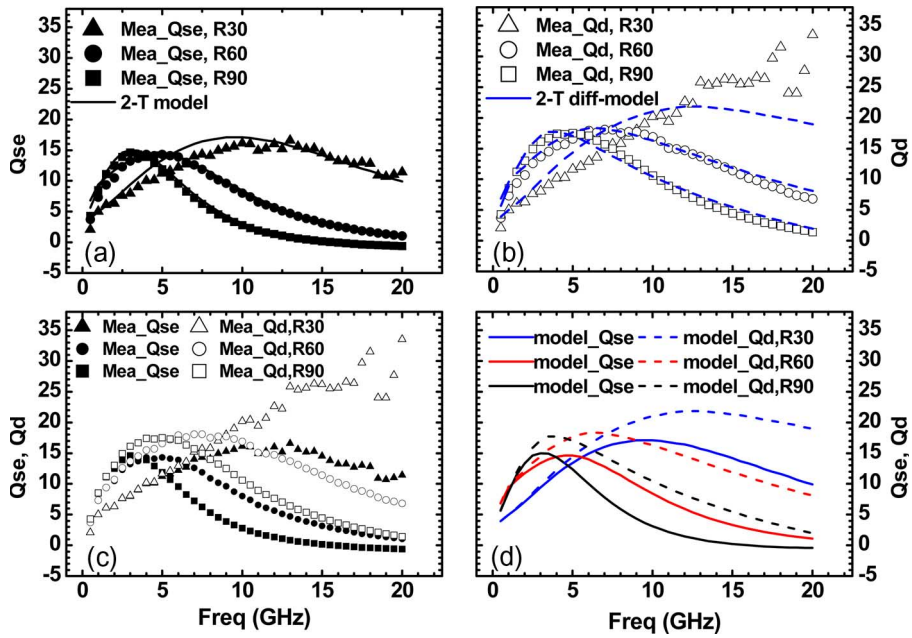

Fig. 13. Comparison between the 2-T model and the measurement for fully symmetric inductors for (a) $Q_{\rm se}$ and (b) Q_d. Comparison of $Q_{\rm se}$ and Q_d between (c) the measurement and (d) the 2-T model.

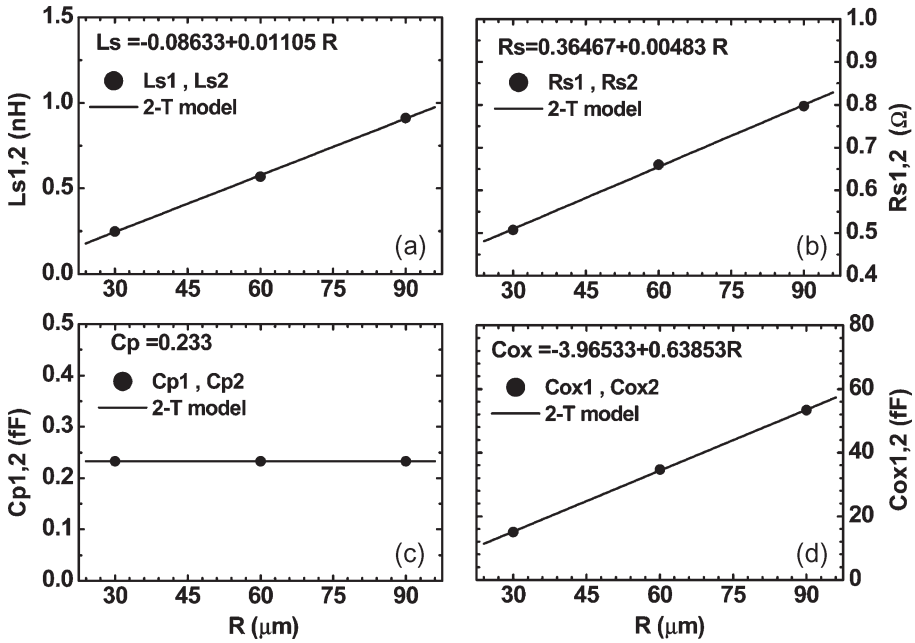

Fig. 14. 2-T model parameters in the spiral coil network versus coil radii. (a) L_S. (b) R_S. (c) C_p. (d) $C_{\rm ox}$.

differential topologies, i.e., $Q_{\rm se}$ and Q_d, over broadband of 20 GHz. However, a somewhat bigger deviation is revealed by the smallest inductor (i.e., $R = 30$ μm) in which the measured Q_d suffers an abnormal increase at a higher frequency. It suggests the challenge in precise de-embedding for the miniaturized devices. Fig. 13(c) and (d) indicates the comparison of $Q_{\rm se}$ and Q_d between the measurement and the 2-T model, respectively. It is interesting to note that Q keeps nearly independent of the single-end or differential excitation in lower frequencies below that corresponding to $Q_{\rm max}$, i.e., $f < f_m$. Getting into a higher frequency region ($f > f_m$), Q improvement that is attributed to a differentially driven operation becomes significant and increases with raising frequencies. The improvement of $Q_{\rm max}$ by around 20%–30% is presented by Q_d compared with $Q_{\rm se}$ for all coil radii. Q improvement is even better than 100% over a broader bandwidth beyond $f_m(Q_{\rm max})$. Note that simple formulas for $Z_{\rm se}$ and Z_d under very low and very high frequencies can be derived from the 2-T model equivalent circuit analysis. In this way, the enhancement of Q_d over $Q_{\rm se}$ and its frequency-dependent feature can be

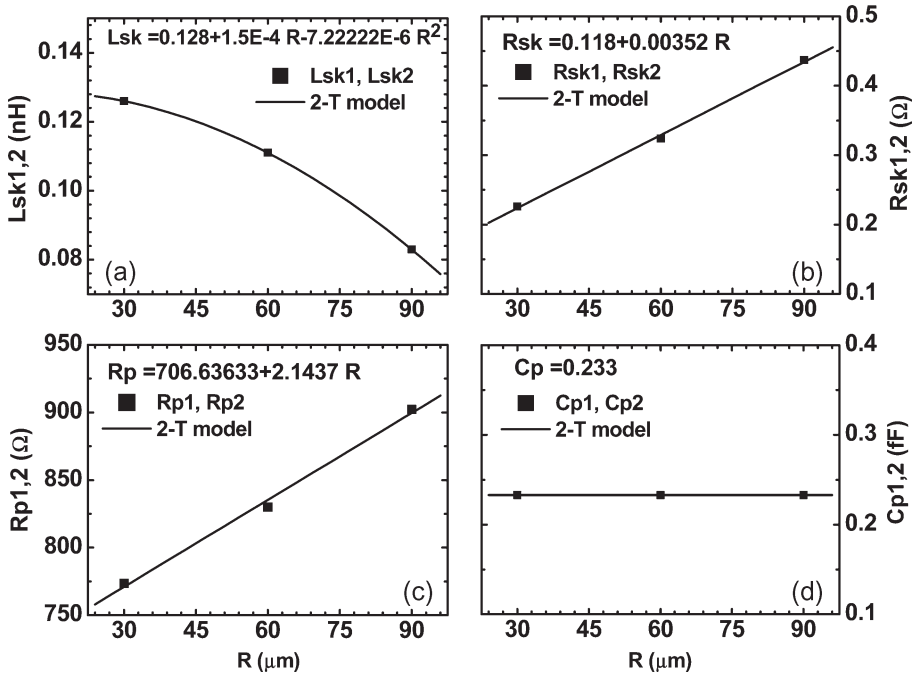

Fig. 15. 2-T model parameters in the spiral coil network versus coil radii. (a) $L_{\rm sk}$. (b) $R_{\rm sk}$. (c) R_p. (d) C_p.

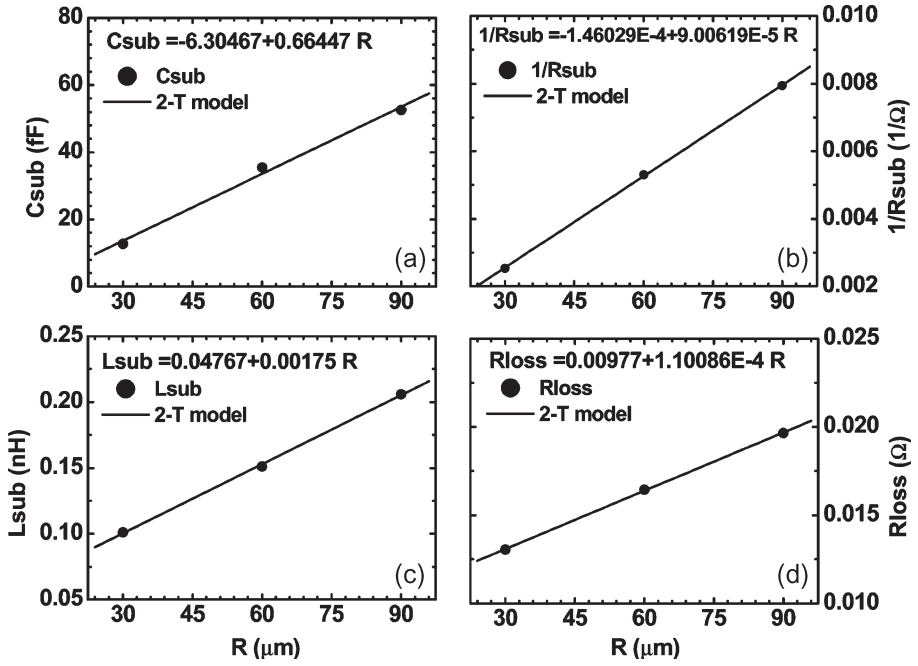

Fig. 16. 2-T model parameters in the substrate network versus coil radii. (a) $C_{\rm sub}$. (b) $1/R_{\rm sub}$. (c) $L_{\rm sub}$. (d) $R_{\rm loss}$.

consistently predicted. As a result, it is proven that a single set of model parameters can be realized by our 2-T model to fit both single-end and differential operations.

C. 2-T Model Scalability

Another important feature is the good scalability with respect to dimensions for all model parameters. Fig. 14 presents a good match with a linear function of coil radii R for four of the model parameters in the spiral coil RLC network, i.e., L_S, R_S, C_p, and $C_{\rm ox}$. All four parameters increase with R. Fig. 15 demonstrates the results for other three parameters in the spiral coil RLC network, i.e., $L_{\rm sk}$, $R_{\rm sk}$, and R_p. Note that $R_{\rm sk}$ and R_p increase with the coil radius following a linear function, whereas $L_{\rm sk}$ decreases according to a parabolic function of R. The larger $L_{\rm sk}$ that is associated with the smaller R suggests that the smaller inductors with smaller coil radii may suffer a worse proximity effect due to the magnetic field coupling of the closely placed coils in the fully symmetric inductor. Fig. 16 indicates the excellent fit by a linear function for the following

substrate network-involved model parameters: $C_{\rm sub}$, $1/R_{\rm sub}$, $L_{\rm sub}$, and $R_{\rm loss}$. The proven scalability suggests that this 2-T model can be used for prelayout simulation and optimization.

VI. Conclusion

A broadband and scalable 2-T model has been developed for accurate simulation of on-chip fully symmetric inductors. A single set of model parameters can fit both single-ended and differentially driven operations. The broadband accuracy is proven by a good match with S-parameters, $L(\omega)$, $Re(Z_{\rm in})$, and $Q(\omega)$ over frequencies up to 20 GHz. The scalability is justified by good fitting with either a linear or a parabolic function of coil radii. This 2-T model consistently predicts $Q_{\max}$ enhancement by 20%–30% for the symmetric inductors under a differential operation. This Q improvement is even better than 100% over broader frequencies beyond $f_m(Q_{\max})$. The scalable model can facilitate an optimal design of symmetric inductors through model parameters that are relevant to various geometries. Furthermore, the broadband accuracy proven by both single-end and differential excitations can improve RF circuit simulation accuracy that is demanded by a broadband design.

Acknowledgment

The authors would like to thank the helpful support from Chip Implementation Center (CiC) for providing the simulation environment and NDL RF Laboratory for RF device measurement. Also, the authors would like to acknowledge the budget support from the Nanoelectronic and Information System Research Center.

References

[1] M. Tiebout, "Low-power low-phase-noise differentially tuned quadrature VCO design in standard CMOS," *IEEE J. Solid-State Circuits*, vol. 36, no. 7, pp. 1018–1024, Jul. 2001.

[2] M. Tiebout, "A CMOS fully integrated 1 GHz and 2 GHz dual band VCO with a voltage controlled inductor," in *Proc. ESSCIRC*, 2002, pp. 799–802.

[3] T.-Y. Lin, Y.-Z. Juang, H.-Y. Wang, and C.-F. Chiu, "A low power 2.2–2.6 GHz CMOS VCO with a symmetrical spiral inductor," in *Proc. ISCAS*, 2003, pp. 641–644.

[4] S. Raman, D. I. Sanderson, and A. S. Klein, "Design considerations for monolithic Si-based RF VCOs in wireless single-chip systems," in *Proc. IEEE Top. Conf. Wireless Commun. Technol.*, 2003, pp. 172–174.

[5] R. L. Bunch, D. I. Sanderson, and S. Raman, "Quality factor and inductance in differential IC implementations," *IEEE Microw. Mag.*, vol. 3, no. 2, pp. 82–92, Jun. 2002.

[6] M. Danesh, J. R. Long, R. A. Hadaway, and D. L. Harame, "A Q-factor enhancement technique for MMIC inductors," in *Proc. IEEE MTT Symp. Dig.*, Jun. 1998, pp. 183–196.

[7] J. R. Long, "Monolithic transformers for silicon RFIC design," *IEEE J. Solid-State Circuits*, vol. 35, no. 9, pp. 1368–1382, Sep. 2000.

[8] M. T. Reiha, T.-Y. Choi, J.-H. Jeon, S. Mohammadi, and L. P. B. Katehi, "High-Q differential inductors for RFIC design," in *Proc. 33rd Eur. Microw. Conf.*, Munich, Germany, 2003, pp. 127–130.

[9] M. Politi, V. Minerva, and S. C. d'Oro, "Multi-layer realization of symmetric differential inductors for RF silicon ICs," in *Proc. 33rd Eur. Microw. Conf.*, Munich, Germany, 2003, pp. 159–162.

[10] H. Y. D Yang, "Design considerations, of differential inductors in CMOS technology for RFIC," in *Proc. IEEE RFIC Symp. Dig.*, Jun. 2004, pp. 449–452.

[11] J.-H. Gau, S. Sang, R.-T. Wu, F.-J. Shen, H.-H. Chen, A. Chen, and J. Ko, "Novel fully symmetrical inductor," *IEEE Electron Device Lett.*, vol. 25, no. 9, pp. 608–609, Sep. 2004.

[12] M. Danesh and J. R. Long, "Differentially driven symmetric microstrip inductors," *IEEE Trans. Microw. Theory Tech.*, vol. 50, no. 1, pp. 332–341, Jan. 2002.

[13] J.-C. Guo and T.-Y. Tan, "A broadband and scalable model for on-chip inductors incorporating substrate and conductor loss effects," *IEEE Trans. Electron Devices*, vol. 53, no. 3, pp. 413–421, Mar. 2006.

Jyh-Chyurn Guo received the B.S.E.E. and M.S.E.E. degrees from the National Tsing-Hua University, Hsinchu, Taiwan, R.O.C., in 1982 and 1984, respectively, and the Ph.D. degree in electronics engineering from the National Chiao-Tung University (NCTU), Hsinchu, in 1994.

She was in the semiconductor industry with a major focus on device design and VLSI technology development for more than 19 years. In 1984, she joined the Electronics Research and Service Organization of the Industrial Technology Research Institute, where she was engaged in semiconductor integrated circuit technologies with a broad scope to cover high-voltage and high-power submicron project, high-speed SRAM technologies, etc. From 1994 to 1998, she was with Macronix International Corporation, where she was engaged in the high-density and low-power Flash memory technology development. In 1998, she joined the Vanguard International Semiconductor Corporation, where she assumed the responsibility of Device Department Manager for advanced DRAM device technology development. In 2000, she joined Taiwan Semiconductor Manufacturing Company, where she served as a Program Manager in charge of the 0.1-μm logic CMOS FEOL, high-performance analog, and RF CMOS technology development. In 2003, she was an Associate Professor in the Department of Electronics Engineering, NCTU, where she is currently a Professor. She is the author or coauthor of near 50 technical papers and is the holder of 12 international patents in her professional field. Her current research interests cover RF CMOS and high-performance analog device design and modeling, novel nonvolatile memory technology, and device integration technology for SOC.

Teng-Yang Tan was born in Taichung, Taiwan, R.O.C., in 1981. He received the M.S. degree in electronics engineering from the National Chiao-Tung University, Hsinchu, Taiwan, R.O.C., in 2006.

His current research interests focus on RF passive device modeling and characterization.